A Practical Position Sensorless Control of Long-Cable-Fed PMSM Drives with a Sine-wave Filter for Electrical Submersible Pumps

Hanyoung Bu[1] and Younghoon Cho[1]

[1] The Department of Electrical and Electronics Engineering, Konkuk University, Seoul, Republic of Korea

***Abstract*-- This paper proposes a practical position sensorless control for electrical submersible pump (ESP) application with a sine-wave filter. In long-cable-fed PMSM drives, it is hard to install sensors at motor-side due to digital signal latency with the long signal cable and inconsistent source for sensors. Therefore, voltage and current correction method is proposed using the output of the sine-wave filter. Then, since the motor in the ESP system can be easily overheated by oil thermal field, an adaptive cable-PMSM coupled *d-q* axis equivalent model derived considering the temperature rise. The speed control performance and load torque-speed transient performance are improved using the proposed sensorless control method. The experimental results show the validity of the effectiveness of the proposed method both both dynamic response and steady-state.**

***Index Terms*—Long-cable-fed PMSM drives, sine-wave filter, voltage and current corrections at motor-side, temperature rise in oil fluid**

I. INTRODUCTION

Permanent magnet synchronous motors (PMSMs) are widely used in applications such as electric vehicles and actuators due to high power and high efficiency. Meanwhile, in long-cable-fed PMSM drives, the motor may be located at a long distance from the power conversion system because of the limitations of the installation environments. From the long distance, long-cable-fed PMSM drives have several limitations. First, the longer the length of the cable, the larger an overvoltage at motor-side. Theoretically, the magnitude of the overvoltage may reach within 2 to 3 times the dc-link voltage [1], [2]. If the overvoltage at motor-side exceeds the insulation voltage between stator windings in the motor, it may cause partial discharge which results in a breakdown [3]-[5]. To solve this problem, companies that vend the inverters for operating the motor recommend maximum cable length using output filters for commercial motor drives [6]-[8]. Although the recommendations are different for each companies, the longest cable length can be utilized using a sine-wave filter. Secondly, signal latency from the sensors at motor-side and instability of power source from a main controller may be a problem for real-time inverter-duty control. Third, harsh environments where the motor is installed can increase temperature on the cable and the motor. Especially, applications where the motor is placed underground such as an electrical submersible pumps (ESP) are weak to these environments [9], [10]. From the limitations, several sensorless control methods for long-cable-fed PMSM systems have been studied [11]-[14].

In [11], a MTPA control using the closed loop observer based system inductance and speed estimation is used for subsea applications. However, the method has the steady-state error in estimated rotor angle and the slow dynamic response. In [12], a Luenberger observer is used to estimate the back-EMF for linear ESP systems. However, the experiments are carried out using the winding resistors and inductors instead of the long cable. Then, the middle point voltage of the cable is used for back-EMF estimation, which is not suitable for practical motor operation. In [13], a seamless transition scheme for ESP systems is introduced. The speed correction term is only effective in the transient and the smooth transition is not always performed according to the open-loop position. Meanwhile, common problem for the conventional studies is that the sensorless control methods use voltages and currents at motor-side. It is not practical considering the limitations of long-cable-fed system.

In this article, a practical position sensorless control of long-cable-fed PMSM drives is proposed. Voltages and currents at motor-side are corrected by using the output voltages and currents of the sine-wave filter. An adaptive cable-PMSM coupled *d-q* axis equivalent model is introduced considering temperature rise in ESP system. The proposed sensorless control method enhances the performances in speed control and load torque-speed transient response. The effectiveness of the proposed sensorless control method is verified through the experiments in both dynamic response and steady-state.

II. CONSIDERATIONS OF LONG-CABLE-FED PMSM SYSTEM

A. Voltage and current corrections at motor-side

Fig. 1 shows the lumped T-net cable-motor model which consists of three cable impedances, motor impedance and back-emf. *j* denotes any one of the three phases a, b, c. The impedances in the lumped T-net cable-motor model are expressed using the telegrapher's equations as follow:

$$Z_{t1}(s) = Z_0(s)[\coth(\gamma_0(s)d) - \operatorname{csch}(\gamma_0(s)d)] \quad (1)$$

$$Z_{t2}(s) = Z_0(s)[\coth(\gamma_0(s)d) - \operatorname{csch}(\gamma_0(s)d)] \quad (2)$$

$$Z_{t12}(s) = Z_0 \operatorname{csch}(\gamma_0(s)d) \quad (3)$$

$$Z_{mot}(s) = R_s + sL_s \quad (3)$$

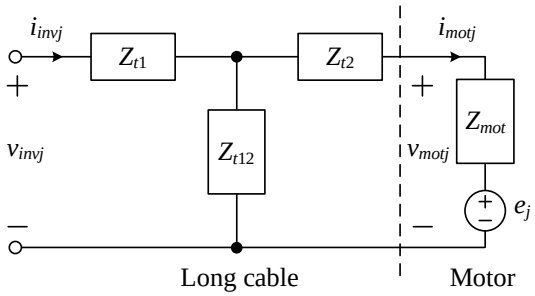

Fig. 1. Lumped T-net cable-motor model.

$$Z_e(s) = \psi_f \omega_r \tag{3}$$

where

$$\gamma_0(s) = \sqrt{(r+sl)(g+sc)} \tag{4}$$

is the propagation coefficient,

$$Z_0(s) = \sqrt{(r+sl)/(g+sc)} \tag{5}$$

is the characteristics impedance. d is the length of the cable. r, l, g, and c are the cable resistance, cable inductance, cable conductance, and cable capacitance per unit length respectively. R_s, L_s, ψ_f and ω_r are the stator resistance, the stator inductance, the magnet flux linkage, and the electrical angular velocity.

From Fig. 1, transfer functions between the inverter-side current and the motor-side current and between the inverter-side voltage and the motor-side voltage are derived as follow:

$$G_{icor}(s) = \frac{i_{motj}(s)}{i_{invj}(s)} = \frac{Z_{t12}}{(Z_{t12}+Z_{t1}+Z_{mot}+Z_e)} \tag{6}$$

$$G_{vcor}(s) = \frac{v_{motj}(s)}{v_{invj}(s)} = \frac{Z_{t12}(Z_{mot}+Z_e)}{Z_{eq}(Z_{t12}+Z_{t2}+Z_{mot}+Z_e)} \tag{7}$$

Fig. 2 and Fig. 3 show the frequency responses of $G_{icor}(s)$ and $G_{vcor}(s)$. From Fig. 2, although the magnitude decreases after the resonance frequency, as the operating speed of the low-voltage inverter motor used in the paper does not exceed 200Hz, the differences between the inverter-side and motor-side current is nearly zero. As similar to the results in Fig. 2, the result of Fig. 3 shows that the differences between the inverter-side and motor-side voltage within the operation range is also zero. However, in actual long-cable-fed system, the motor-side voltage decreases by the cable resistance. The result of Fig. 3 does not reflect this phenomenon. Accordingly, the lumped T-net cable-motor model should be refined to reflect the actual voltage drop.

Fig. 4 shows the lumped T-net cable-motor low-frequency model. d is the length of the cable. The sine-wave filter is added to the lumped T-net cable-motor model and the impedance Z_{t1} and Z_{t2} are substituted into resistance components and Z_{t12} is replaced into capacitance component. The sine-wave filter makes overvoltage mitigation at motor-side and low-frequency analysis on Fig. 4 possible. Meanwhile, the transfer function between the inverter-side and motor-side voltage within low-frequency region is rewritten as follow:

$$G_{vest}(s) = \frac{v_{motj}}{v_{Cfj}} = \frac{Z_{Cf}}{Z_{p1}+Z_{Cf}} \frac{1}{Z_{p2}} \frac{Z_{t12}(Z_{mot}+Z_e)}{Z_{t12}+Z_{t2}+Z_{mot}+Z_e}$$

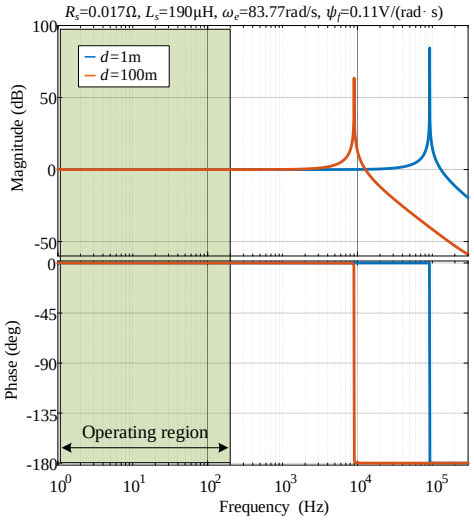

Fig. 2. Frequency responses of $G_{icor}(s)$ for different cable lengths.

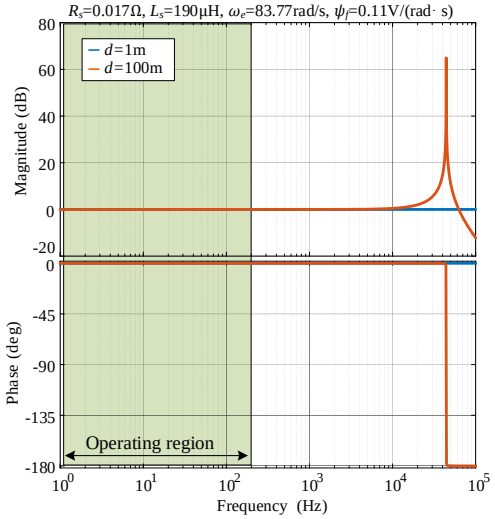

Fig. 3. Frequency responses of $G_{vcor}(s)$ for different cable lengths.

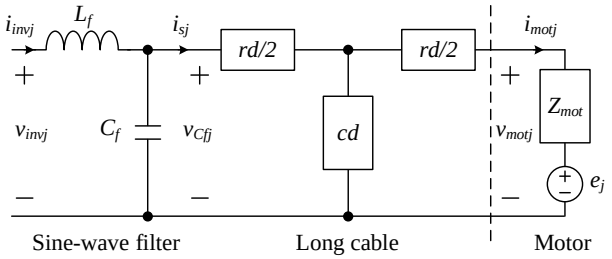

Fig. 4. Lumped T-net cable-motor low-frequency model.

$$Z_{p1} = Z_{t1} + \frac{Z_{t12}(Z_{t2}+Z_{mot}+Z_e)}{(Z_{t12}+Z_{t2}+Z_{mot}+Z_e)}$$
$$Z_{p2} = Z_{Lf} + \frac{Z_{Cf}Z_{p1}}{Z_{Cf}+Z_{p1}} \tag{8}$$

where Z_{Lf} is the inductor impedance of the sine-wave filter and Z_{Cf} is the capacitor impedance of the sine-wave filter.

Fig. 5 shows the Frequency responses of $G_{vcor}(s)$ and $G_{vest}(s)$. Unlike Fig. 3, the magnitude reduction at motor-side caused by the cable voltage drop occurs within low-frequency region. Therefore, the lumped T-net cable-

motor low-frequency model is best option for practical long-cable-fed PMSM drives.

Meanwhile, the transfer function between the inverter-side and motor-side voltage of (8) has a few limitations. First, the result of Fig. 5 differs according to the synchronous angular velocity ω_e. The mathematical model with the sine-wave filter in synchronous d-q frame is derived as below:

$$\begin{bmatrix} v_{invd} \\ v_{invq} \end{bmatrix} = \begin{bmatrix} v_{Cd} \\ v_{Cq} \end{bmatrix} + L_f \begin{bmatrix} p & -\omega_e \\ \omega_e & p \end{bmatrix} \begin{bmatrix} i_{invd} \\ i_{invq} \end{bmatrix}$$
$$\begin{bmatrix} i_{invd} \\ i_{invq} \end{bmatrix} = \begin{bmatrix} i_{sd} \\ i_{sq} \end{bmatrix} + C_f \begin{bmatrix} p & -\omega_e \\ \omega_e & p \end{bmatrix} \begin{bmatrix} v_{Cd} \\ v_{Cq} \end{bmatrix} \quad (9)$$

where p is the derivative operator, L_f and C_f represent the sine-wave filter inductance and capacitance, v_{invdq} and i_{invdq} represent the d-q axis inverter-side voltages and currents, v_{Cdq} represents the sine-wave filter capacitor voltages and i_{sdq} represents the d-q axis currents after the sine-wave filter inductor, respectively. From (9), the voltage and current terms with ω_e are included and the terms are also included in (8). Fig. 6 shows that as the synchronous angular velocity increases, the magnitude of the voltage drop decreases within the operation region. Secondly, (8) does not consider the current deviation in the cable. Accordingly, (8) shows the characteristics of the case where the synchronous angular frequency and the current in the cable are constant. However, in actual motor operating conditions, as the motor speed and the load torque change, it is difficult to apply (8) in actual motor drive system.

In the paper, the voltage correction equation is derived considering the cable resistance and the current variation in the cable as follow:

$$v_{motj\_corr} = v_{Cj} - rdi_{sj} \quad (10)$$

From Fig. 6, since the phase variation of the frequency response is almost none within operating region, the correction voltage at motor-side can be written only for voltage magnitude except the phase change.

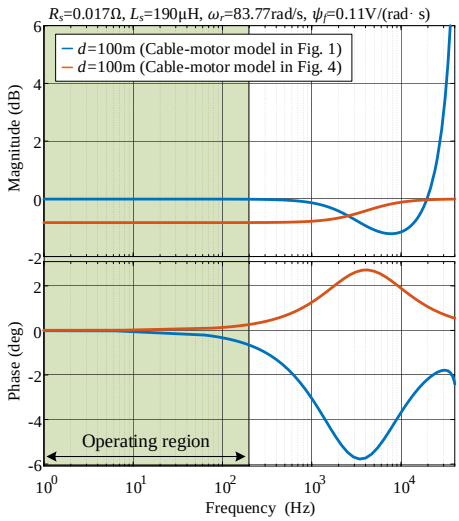

Fig. 5. Frequency responses of $G_{vcor}(s)$ and $G_{vest}(s)$.

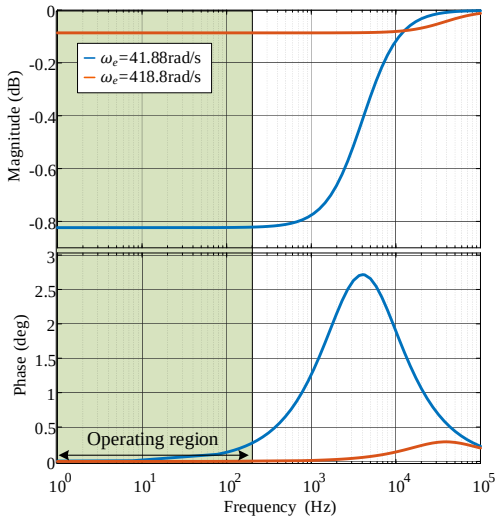

Fig. 6. Frequency response of $G_{vest}(s)$ according to ω_e.

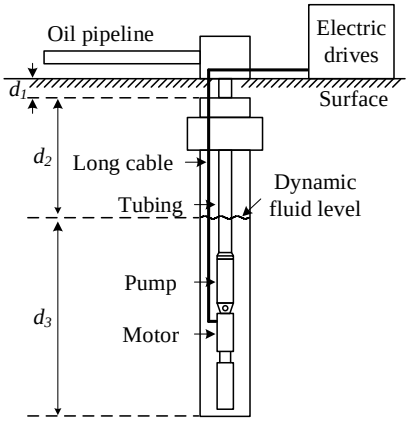

Fig. 7. Overall diagram for typical ESP system.

B. *Practical considerations for ESP system*

The ESP system consist of multiple centrifugal pump stages with a vertical arrangement as shown in Fig. 7. By the field survey of the ESP, the temperature is different according to the field characteristics [2]. The thermal field can be divided into three regions where the surface layer d_1, the gradient layer d_2, and the oil layer d_3.

Especially, in the oil thermal field in d_3 where the motor is placed, the temperature varies rapidly due to high thermal conductivity and heat capacity compared to other regions resulting in the variation of the cable resistance. Therefore, it is adequate to add the cable resistance into the PMSM equivalent model considering the impact of the oil thermal field. It is quite reasonable because oil thermal conductivity is 8 times larger than air thermal conductivity resulting in temperature increase in oil field than other regions dramatically. Fig. 8 shows the adaptive cable-PMSM coupled equivalent model. The difference from the conventional PMSM circuit is that a cable resistance R_T is added to stator resistance R_w. The cable resistance and the stator resistance caused by increased temperature are calculated according to the equations summarized in Appendix.

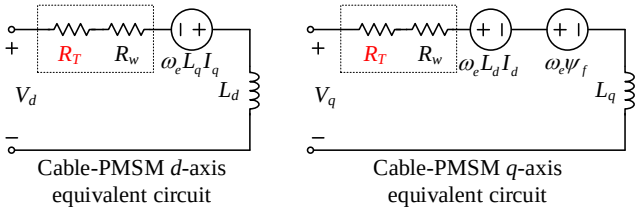

Cable-PMSM *d*-axis equivalent circuit

Cable-PMSM *q*-axis equivalent circuit

Fig. 8. Adaptive cable-PMSM coupled *d*-*q* axis equivalent model.

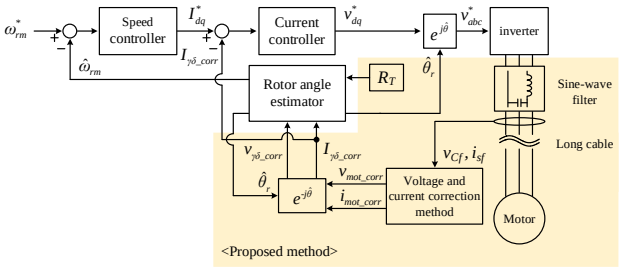

Fig. 9. Overall diagram for typical ESP system.

III. Proposed Sensorless Control for Long-Cable-Fed System

A. Speed control performance

Fig. 9 shows the proposed sensorless control block diagram. From the output voltage and currents of the sine-wave filter, the voltages and currents are corrected. Unlike the conventional sensorless control which uses the voltage reference from the current controller and measured current, the proposed sensorless control uses the correction voltages and currents for the rotor angle estimator. Then, the cable resistor acts like an active damping resistor used to artificially adjust the electrical damping of the system. Fig. 10 shows the speed control block diagram for long-cable-fed system. The transfer functions in Fig. 10 are defined as follow:

$$G_{sc}(s) = k_{ps} + \frac{k_{is}}{s} \tag{11}$$

$$G_{cc}(s) = k_{pc} + \frac{k_{ic}}{s} \tag{12}$$

$$G_d(s) = e^{-1.5sT_s} \tag{13}$$

$$G_{iv}(s) = \frac{I_{\gamma\delta\_sel}}{v_{invdq}} = \frac{Z_{Cf} \cdot Z_{t12}}{(Z_{p1} + Z_{Cf})(Z_{t12} + Z_{t2} + Z_m + Z_e)Z_{p2}} \tag{14}$$

where k_{ps} and k_{is} are the proportional and integral gain for the speed controller $G_{sc}(s)$, k_{pc} and k_{ic} are the proportional and integral gain for the current controller $G_{cc}(s)$, T_s is the sampling period and $G_{iv}(s)$ is the system transfer function. From (11)-(14), the closed-loop transfer function for the speed controller $G_{\omega\_cl}(s)$ is defined as follow:

$$G_{\omega\_cl}(s) = \frac{\omega_{rm}}{\omega_{rm}^*} = \frac{T_{sc\_op}(s)}{1 + T_{sc\_op}(s)}$$

$$T_{sc\_op}(s) = G_{sc}(s) G_{cc\_cl}(s) \frac{K_T}{Js + B} \tag{15}$$

$$G_{cc\_cl}(s) = \frac{G_{cc}(s) G_d(s) G_{iv}(s)}{1 + G_{cc}(s) G_d(s) G_{iv}(s)}$$

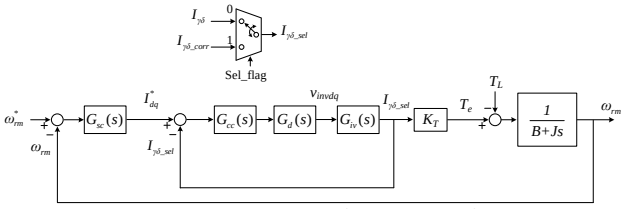

Fig. 10. Speed control block diagram for long-cable-fed system.

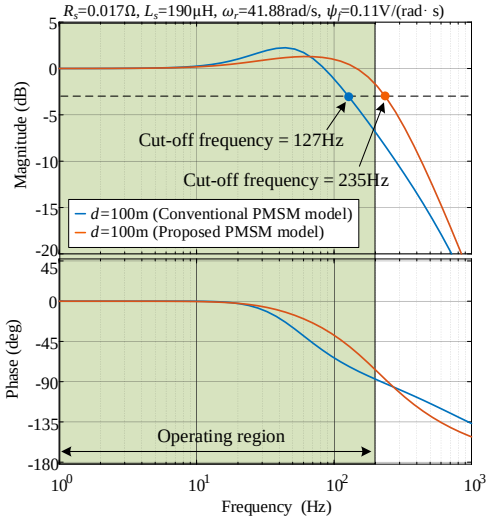

Fig. 11. Frequency responses for closed-loop transfer function for the speed controller.

where $G_{cc\_cl}(s)$ is the closed-loop transfer function for current controller and $T_{sc\_op}(s)$ is the open-loop transfer function for the speed controller. Fig. 11 shows that the cut-off frequency is placed within the operating region using the conventional PMSM model. This result can not satisfy the bandwidth requirement of the speed controller. However, the cut-off frequency is extended above the operating region using the proposed PMSM model. Thus, the proposed sensorless control is effective as the length of the cable is increased.

B. Load torque-speed transient performance

From Fig. 10, the load torque-speed transfer function $G_T(s)$ is obtained as follow:

$$G_T(s) = \frac{\omega_{rm}}{T_L} = \frac{\frac{1}{Js + B}}{1 + T_{sc\_op}(s)} \tag{16}$$

Fig. 12 shows the frequency responses of (16). It is ideal that the change in speed should be minimized even when the load torque changes to obtain the robustness of the speed control. When the conventional sensorless control is used, the speed is changed significantly within a certain frequency region where the control system becomes very unstable. However, when the proposed sensorless control is used, the magnitude of the frequency response is below 0 dB. It means that the control system becomes stable in whole frequency region.

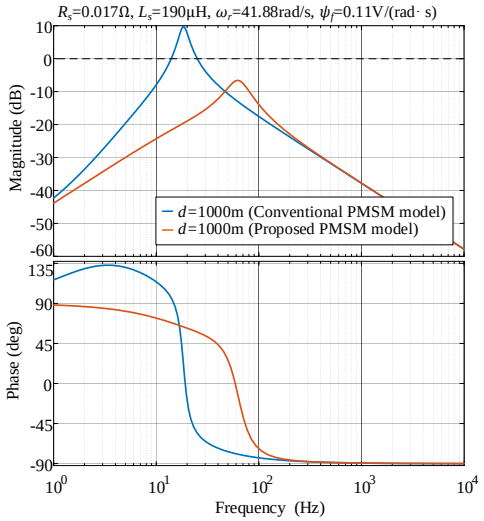

Fig. 12. Frequency responses for load torque-speed transfer function.

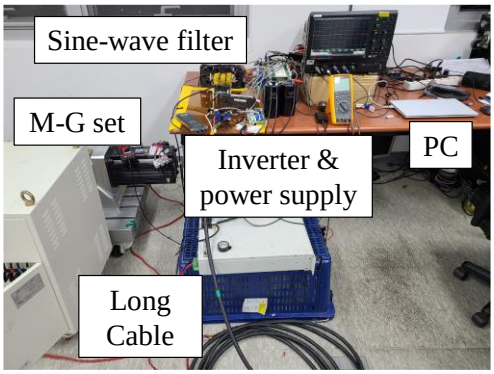

Fig. 13. Experimental configuration.

IV. Experimental Results

Experiments have been performed to verify the effectiveness of the proposed sensorless control method. Fig. 13 shows the experimental configuration. From the calculation procedures in Appendix, the cable resistance and the stator resistance are calculated as 0.43 Ω and 0.022 Ω. Since the experiment was carried out for academic study, it is hard to implement the actual ESP system with oil fluid. Alternatively, the length of the cable was extended to 100m to match the increased cable resistance of 0.43 Ω.

Fig. 14 shows the deceleration operation from 750 rpm to 60 rpm with 10% of the rated torque. There are significant differences in position errors and δ-axis mean EMF values as the operating speed decreases. The position errors between the estimated rotor angle and the real rotor angle at 60rpm are 1.5rad for fig.(a) and 0.75rad for fig.(b). When the proposed sensorless control is used, the position error decrease by 50%. The δ-axis mean EMF values at 60rpm are 10.5V for fig.(a) and 3.8rad for fig.(b). The δ-axis mean EMF value is much closer to the real value when the proposed sensorless control is used.

Fig. 15 shows the steady-state speed and position estimation performance at 100 rpm with 10% of the rated torque. when the proposed method is applied, it shows better speed and position estimation performances in

TABLE I
Experimental Parameters

Parameter	Value
DC-link voltage (V_{dc})	300 V
Switching frequency (f_{sw})	10 kHz
Stator resistance (R_s)	0.017 Ω
d- and q-axis inductance (L_d, L_q)	190 μH
Number of poles (P)	8
Magnet flux linkage (ψ_f)	0.11 V/(rad/s)
Sine-wave filter inductance (L_f)	200 μH
Sine-wave filter capacitance (C_f)	10 μF
Cable length (d)	100 m
Cable resistance (r)	4.5 mΩ/km

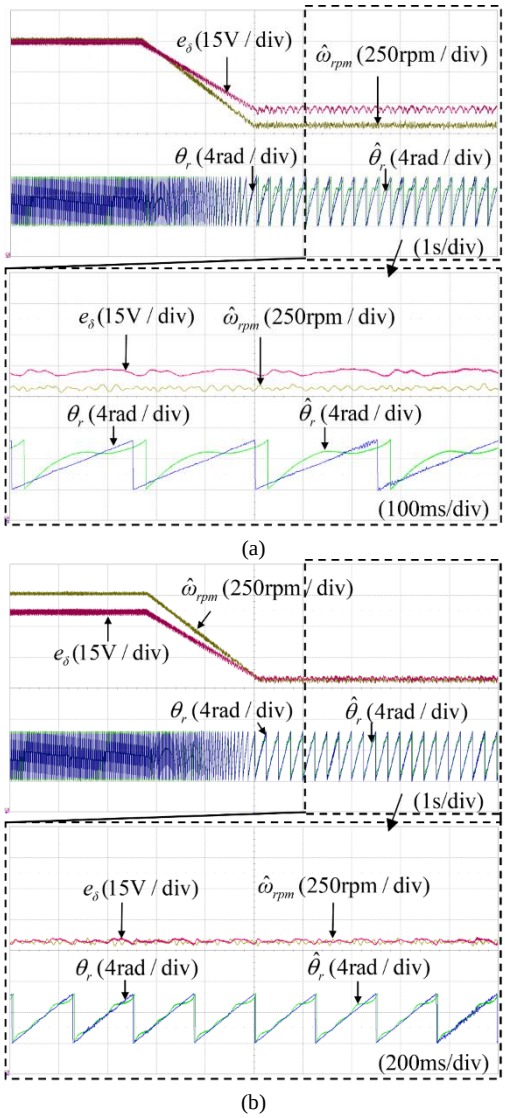

Fig. 14. Deceleration experimental results. (a) Using conventional sensorless control. (b) Using proposed sensorless control.

steady-state. The speed fluctuation is decreased by 43%, and position error is decreased by 28%.

Fig. 16 compares speed dynamic responses with a 10% step load of the rated torque at 100 rpm. As can be seen in Fig. 16(a), the estimation capability is lost when the step load is applied. However, in Fig. 16(b), although the minimum speed reaches 25 rpm, the speed estimation performance is recovered in a steady state.

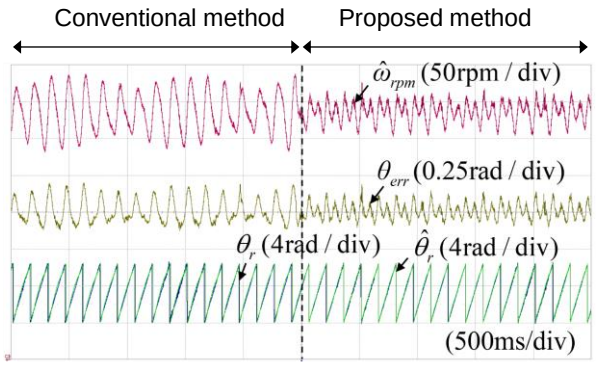

Fig. 15. Steady-state speed and position estimation performance with and without proposed method.

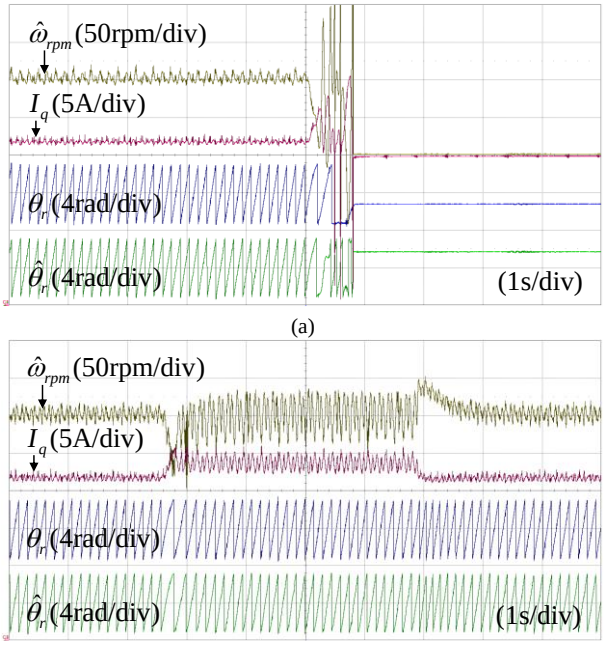

Fig. 16. Speed responses when step load is applied. (a) Using conventional sensorless control. (b) Using proposed sensorless control.

Thus, the experimental results verify that the stability and robustness for speed and position estimation are much better in both dynamic response and steady-state.

V. Conclusions

This paper discussed a practical sensorless algorithm for long-cable-fed motor drives for ESP system. Voltage and current correction method at motor-side was proposed using a lumped T-net cable-motor low-frequency model. Then, an adaptive cable-PMSM coupled *d-q* axis equivalent model is introduced considering practical temperature rise in ESP system. The speed control performance and load torque-speed transient performance were improved by using the proposed sensorless control. The experimental results verified the position and EMF estimation performances are improved in both dynamic response and steady state.

Appendix

The cable sectional area is s_{cable} is 4 mm^2 and the cable length l_{cable} in d_3 is 70 m used in this paper. The parameters for calculating the temperature rise are described in Table II. The cable resistance and the stator resistance in the ESP system considering the temperature rise are calculated as follow [15]:

$$r = \rho \frac{l_{cable}}{s_{cable}} \tag{17}$$

$$R_T = r[1 + k_a(T_f - 25)] \tag{18}$$

$$R_w = \frac{T_w + K}{T_0 + K} R_s \tag{19}$$

where r is the cable resistance at 25 °C, k_a is the temperature coefficient of 0.01, T_f is the average fluid temperature in the ESP casing, R_w is the stator resistance at temperature T_w, K is the temperature coefficient of resistance of 234.5 for 100% conductivity copper, R_s is the initial stator resistance at a at 25 °C of T_0 and T_w is the temperature of the stator widings.

TABLE II
Parameters for Calculating Temperature Rise

Parameter	Value
Pump head (H)	2740 m
Specific heat of light oil (c)	0.5 BTU/lb/°F
Motor efficiency (η_m)	0.9
Pump efficiency (η_p)	0.6
Motor BHP (BHP)	60 HP
Motor length (L_{mot})	1.5 m
Motor outer diameter (d_{mot})	0.11 m
Ambient temperature in annulus (T_a)	150 °F

Acknowledgment

This work was supported by the Technology Innovation Program(No. 20010965, Development of Electronic Current Voltage Transformer and Spacer based on Eco-friendly Solid Insulation) funded by the Ministry of Trade, Industry & Energy(MOTIE) and Korea Evaluation Institute of Industrial Technology(KEIT) of the Republic of Korea.

References

[1] L. Wang, C. Ngai-Man Ho, F. Canales and J. Jatskevich, "High-Frequency Modeling of the Long-Cable-Fed Induction Motor Drive System Using TLM Approach for Predicting Overvoltage Transients," *IEEE Trans. Power Electron.*, vol. 25, no. 10, pp. 2653-2664, Oct. 2010.

[2] Y. Xu et al., "Impact of High Switching Speed and High Switching Frequency of Wide-Bandgap Motor Drives on Electric Machines," in *IEEE Access*, vol. 9, pp. 82866-82880, 2021.

[3] S. Gulur, V. Mahadeva Iyer and S. Bhattacharya, "A CM Filter Configuration for Grid-Tied Voltage Source Converters," *IEEE Trans. Ind. Electron.*, vol. 67, no. 10, pp. 8100-8111, Oct. 2020.

[4] A. Ganjavi, F. Zare, D. Kumar, A. M. Abbosh, K. S. Bialkowski and P. Davari, "Mathematical Model of Common-Mode Sources in Long-Cable-Fed Adjustable Speed Drives," *IEEE Trans. Ind. Appl.*, vol. 58, no. 2, pp. 2013-2028, March-April 2022.

[5] N. Hanigovszki, J. Landkildehus, G. Spiazzi and F. Blaabjerg, "An EMC evaluation of the use of unshielded motor cables in AC adjustable speed drive applications," *IEEE Trans. Power Electron.*, vol. 21, no. 1, pp. 273-281, Jan. 2006.
[6] Danfoss, “Fact sheet : VLT® dU /dt Filter MCC 102”, 2012
[7] ABB, “Low voltage Industrial performance motors”, 2010
[8] WEG, “Technical Catalogue : Low and High Voltage High Performance Electric Motor Range”
[9] H. Zhang, J. Yu, Q. Jiang, L. Wang and D. Xu, "Research on intelligent power supply control based on sensor-less temperature identification of Electric Submersible Motor," 2015 9th International Conference on Power Electronics and ECCE Asia (ICPE-ECCE Asia), Seoul, Korea (South), pp. 2802-2807, 2015.
[10] L. Wang, D. Jin, H. Zhu and C. Yu, "An Approach For Saving Power of ESM With Long Cable by Control Frequency Based on Sensor-Less Estimating Temperature," *IEEE Trans. Ind. Electron.*, vol. 64, no. 12, pp. 9233-9242, Dec. 2017.
[11] V. Singh, M. G. Majumder, K. Rajashekara and R. P. R. Siddavatam, "Parameter Estimation for Sensorless Position Control of PMSM Drives with Long Cable in Subsea Applications," 2022 International Power Electronics Conference (IPEC-Himeji 2022- ECCE Asia), Himeji, Japan, pp. 384-388, 2022.
[12] H. A. Hussain and H. A. Toliyat, "Position sensorless control of a permanent magnet linear motor connected through a long cable," 2017 IEEE Energy Conversion Congress and Exposition (ECCE), Cincinnati, OH, USA, pp. 830-835, 2017.
[13] J. Liu, T. A. Nondahl, J. Dai, S. Royak and P. B. Schmidt, "A Seamless Transition Scheme of Position Sensorless Control in Industrial Permanent Magnet Motor Drives With Output Filter and Transformer for Oil Pump Applications," *IEEE Trans. Ind. Appl.*, vol. 56, no. 3, pp. 2180-2189, May-June 2020.
[14] L. Ding, Y. W. Li, N. R. Zargari and R. Paes, "Sensorless Control of CSC-Fed PMSM Drives With Low Switching Frequency for Electrical Submersible Pump Application," in IEEE Transactions on Industry Applications, vol. 56, no. 4, pp. 3799-3808, July-Aug. 2020.
[15] G. Takacs, *Electrical Submersible Pumps Manual: Design, Operations, and Maintenance*. Gulf Professional Publishing, 2018.